

Kinetic theory and memory effects of homogeneous inelastic granular gases under nonlinear drag

Alberto Megías¹  Andrés Santos^{2*} 

¹ Departamento de Física, Universidad de Extremadura, E-06006 Badajoz, Spain; albertom@unex.es

² Departamento de Física and Instituto de Computación Científica Avanzada (ICCAEx), Universidad de Extremadura, E-06006 Badajoz, Spain; andres@unex.es

* Correspondence: andres@unex.es

Received: date; Accepted: date; Published: date

Abstract: We study in this work a dilute granular gas immersed in a thermal bath made of smaller particles with nonnegligible masses as compared with the granular ones. The kinetic theory for this system is developed and described by an Enskog–Fokker–Planck equation for the one-particle velocity distribution function. Granular particles are assumed to have inelastic and hard interactions, losing energy in collisions as accounted by a constant coefficient of normal restitution. The interaction with the thermal bath is based on a nonlinear drag force plus a white-noise stochastic force. To get explicit results of the temperature aging and steady states, Maxwellian and first Sonine approximations are developed. The latter takes into account the coupling of the excess kurtosis with the temperature. Theoretical predictions are compared with direct simulation Monte Carlo and event-driven molecular dynamics simulations. While good results for the granular temperature are obtained from the Maxwellian approximation, a much better agreement, especially as inelasticity and drag nonlinearity increase, is found when using the first Sonine approximation. The latter approximation is, additionally, crucial to account for memory effects like Mpemba and Kovacs-like ones.

Keywords: granular gases; kinetic theory; Enskog–Fokker–Planck equation; direct simulation Monte Carlo; event-driven molecular dynamics

1. Introduction

Since the late 20th, the study of granular materials has become of great importance in different branches of science, such as physics, engineering, chemistry, or mathematics, motivated by either fundamental or industrial reasons. It is well known that rapid flows in granular gases in the dilute regime are well described by a modified version of the classical Boltzmann’s kinetic theory for hard particles. The most widely used model for the granular particles is the inelastic hard-sphere (IHS) one, in which particles are assumed to be hard spheres (or, generally, hard d -spheres) that lose energy due to inelasticity, as parameterized by a constant coefficient of normal restitution, α .

Theoretical predictions have been tested by different experimental setups in the freely evolving case [1,2]. However, it is rather difficult to replicate experimentally the latter granular gaseous systems due to the fast freezing implied by the dissipative interactions. Then, injecting energy is very common in granular experiments [3–10]. In addition, granular systems are never found in vacuum on Earth. From a quick but attentive glance at our close environment, grains might be found, for example, in the form of dust suspended in the air, sand or dirtiness diving down or browsing through a river, or even forming part of more complex systems like soils. Therefore, fundamental knowledge about driven granular flows helps the understanding of a great variety of phenomena in nature. This is one of the reasons why the study of driven granular flows becomes quite important, besides its intrinsic interest at physical and mathematical levels. Consequently, modeling driven granular flows constitutes a solid part in granular matter research, with theorists combining different collisional models with distinct interactions with the surroundings [11–20].

Recent works [21–23] introduced a model for a molecular gas in which the interaction of the particles with a background fluid is described by a stochastic force and a drag force whose associated drag coefficient has a quadratic dependence on the velocity modulus. This latter dependence is motivated by situations where the particle masses in the gas and the background fluid are not very disparate [24–26]. The nonlinearity of the drag force implies an explicit coupling of the temperature with higher-order moments of the velocity distribution function (VDF) of the gas, implying the existence of interesting memory effects, such as Mpemba or Kovacs-like ones, as well as nonexponential relaxations [21–23]. On the other hand, the elastic property of the molecular particles implies that the system ends in an equilibrium state described by the common Maxwell–Boltzmann VDF, unlike granular gases, both driven and freely evolving [11,12,14,17,18,27–30], where a coupling of the hydrodynamic quantities with the cumulants of the VDF is always present.

Throughout this work, we study the properties of homogeneous states of a dilute inelastic granular gas immersed in a background fluid made of smaller particles, the influence of the latter on the former being accounted for at a coarse-grained level by the sum of a deterministic nonlinear drag force and a stochastic force. This gives rise to a competition between the pure effects of the bath and the granular energy dissipation. In fact, we have looked into expected nonGaussianities from a Sonine approximation of the VDF, commonly used in granular gases. The theoretical results are tested against computer simulations, with special attention to the steady-state properties and memory effects.

The paper is organized as follows. We introduce the model for this system and the associated kinetic-theory evolution equations in Sec. 2. In Section 3, the Maxwellian and first Sonine approximations are constructed, and the steady-state values are theoretically evaluated. Then, Sec. 4 collects simulation results from the direct simulation Monte Carlo (DSMC) method and the event-driven molecular dynamics (EDMD) algorithm, which are compared to the theoretical predictions for steady and transient states, including memory effects. Finally, in Sec. 5, some conclusions of this work are exposed.

2. The Model

We consider a homogeneous, monodisperse, and dilute granular gas of identical inelastic hard d -spheres of mass m and diameter σ , immersed in a background fluid made of smaller particles. In a coarse-grained description, the interactions between the grains and the fluid particles can be effectively modeled by a drag force plus a stochastic force acting on the grains. If the mass ratio between the fluid and granular particles is not excessively small, the drag force becomes a nonlinear function of the velocity [24–26]. The model, as said in Sec. 1, has previously been studied in the case of elastic collisions [21–23] but not, to our knowledge, in the context of the IHS model. Figure 1 shows an illustration of the system and its modeling.

2.1. Enskog–Fokker–Planck Equation

The full dynamics of the system can be studied from the inelastic homogeneous Enskog–Fokker–Planck equation (EFPE),

$$\partial_t f(\mathbf{v}; t) - \partial_{\mathbf{v}} \left[\xi(v) \mathbf{v} + \frac{\chi^2(v)}{2} \partial_{\mathbf{v}} \right] f(\mathbf{v}; t) = J[\mathbf{v}|f, f], \quad (1)$$

where f is the one-particle VDF, so that $n = \int d\mathbf{v} f(\mathbf{v}; t)$ is the number density, and $J[\mathbf{v}|f, f]$ is the usual Enskog–Boltzmann collision operator defined by

$$J[\mathbf{v}_1|f, f] \equiv \sigma^{d-1} g_c \int d\mathbf{v}_2 \int_+ d\hat{\sigma} (\mathbf{v}_{12} \cdot \hat{\sigma}) \left[\alpha^{-2} f(\mathbf{v}'_1) f(\mathbf{v}'_2) - f(\mathbf{v}_1) f(\mathbf{v}_2) \right]. \quad (2)$$

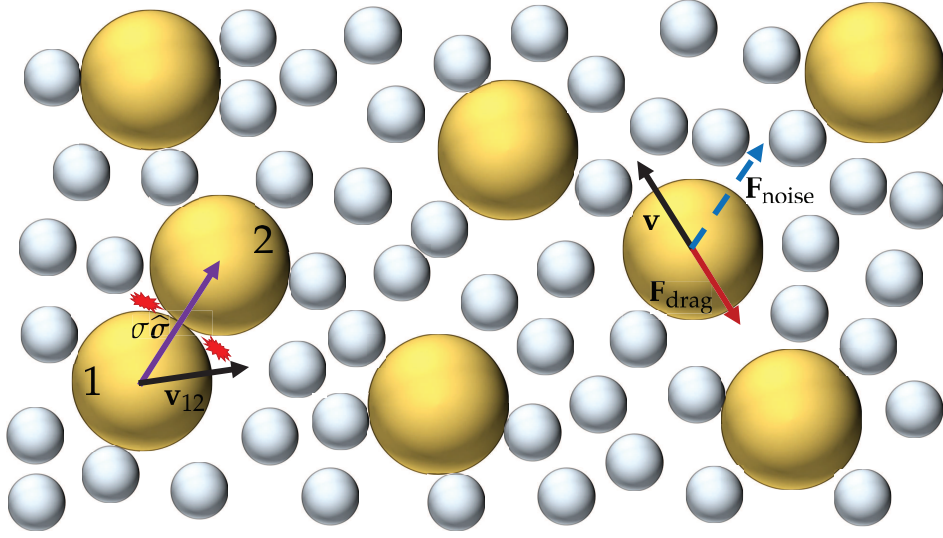


Figure 1. Illustration of the system considered in this paper. A granular gas of hard particles (represented by large yellowish spheres) is coupled to a thermal bath (made of particles represented by the small grayish spheres) via a drag force $\mathbf{F}_{\text{drag}} = -m\zeta(v)\mathbf{v}$, where $\zeta(v)$ is a velocity-dependent drag coefficient, and a stochastic force $\mathbf{F}_{\text{noise}} = m\chi(v)\boldsymbol{\eta}$, where $\boldsymbol{\eta}$ is a Gaussian white-noise term. In addition, the granular particles are subjected to binary inelastic collisions, represented by the red gleam-like lines.

Here, $\mathbf{v}_{12} = \mathbf{v}_1 - \mathbf{v}_2$ is the relative velocity, $\hat{\boldsymbol{\sigma}} = (\mathbf{r}_1 - \mathbf{r}_2)/\sigma$ is the intercenter unit vector at contact, $g_c = \lim_{r \rightarrow \sigma^+} g(r)$ is the contact value of the pair correlation function, $\int_+ d\hat{\boldsymbol{\sigma}} \equiv \int d\hat{\boldsymbol{\sigma}} \Theta(\mathbf{v}_{12} \cdot \hat{\boldsymbol{\sigma}})$, Θ being the Heaviside step-function, and \mathbf{v}_i'' refers to the precollisional velocity of particle i . Within the IHS model, the collisional rules are expressed by [18,30]

$$\mathbf{v}_{1/2}'' = \mathbf{v}_{1/2} \mp \frac{1 + \alpha^{-1}}{2} (\mathbf{v}_{12} \cdot \hat{\boldsymbol{\sigma}}) \hat{\boldsymbol{\sigma}}. \quad (3)$$

In addition, the second term on the right-hand side of Eq. (1) represents the action of a net force $\mathbf{F} = \mathbf{F}_{\text{drag}} + \mathbf{F}_{\text{noise}}$ due to the interaction with the particles of the background fluid. The deterministic nonlinear drag force is $\mathbf{F}_{\text{drag}} = -m\zeta(v)\mathbf{v}$, where the drag coefficient $\zeta(v)$ depends on velocity. In turn, $\mathbf{F}_{\text{noise}} = m\chi^2(v)\boldsymbol{\eta}$ is a stochastic force, where $\chi^2(v)$ measures its intensity and $\boldsymbol{\eta}$ is a stochastic vector with the properties of a zero-mean Gaussian white noise with unit covariance matrix, i.e.,

$$\langle \boldsymbol{\eta}_i(t) \rangle = 0, \quad \langle \boldsymbol{\eta}_i(t) \boldsymbol{\eta}_j(t') \rangle = \mathbb{I} \delta_{ij} \delta(t - t'), \quad (4)$$

where i, j are particle indices and \mathbb{I} is the $d \times d$ unit matrix. The functions $\zeta(v)$ and $\chi^2(v)$ are constrained to follow the fluctuation-dissipation theorem as

$$\chi^2(v) = v_b^2 \zeta(v), \quad (5)$$

$v_b = \sqrt{2T_b/m}$ being the thermal velocity associated with the background temperature T_b .

The drag coefficient ζ is commonly assumed to be independent of velocity. However, a dependence on v cannot be ignored if the mass of a fluid particle is not negligibly smaller than that of a grain [24–26]. The first correction to $\zeta = \text{const}$ is a quadratic term [21–23], namely

$$\zeta(v) = \zeta_0 \left[1 + 2\gamma \left(\frac{v}{v_b} \right)^2 \right], \quad (6)$$

where ξ_0 is the drag coefficient in the zero-velocity limit and γ controls the degree of nonlinearity of the drag force.

2.2. Dynamics

It is well known that, in the case of driven granular gases [11,12,14,17–19], there exists a competition between the loss and gain of energy due to inelasticity and the action of the thermal bath, respectively. This eventually leads the granular gas to a steady state, in contrast to the freely cooling case [18].

The basic macroscopic quantity characterizing the time evolution of the system is the *granular temperature*, defined analogously to the standard temperature in kinetic theory as

$$T(t) = \frac{m}{dn} \int d\mathbf{v} v^2 f(\mathbf{v}; t). \quad (7)$$

While in the case of elastic collisions the asymptotic steady state is that of equilibrium at temperature T_b , so that $\lim_{t \rightarrow \infty} T(t) = T_b$, in the IHS model the steady state is a nonequilibrium one and, moreover, $\lim_{t \rightarrow \infty} T(t) = T^{\text{st}} < T_b$. From the EFPE one can derive the evolution equation of the granular temperature, which is given by

$$\frac{\partial_t T}{\xi_0} = 2(T_b - T) \left[1 + (d+2)\gamma \frac{T}{T_b} \right] - 2(d+2)\gamma \frac{T^2}{T_b} a_2 - \frac{\zeta}{\xi_0} T, \quad (8)$$

where

$$\zeta(t) \equiv -\frac{m}{dT(t)n} \int d\mathbf{v} v^2 J[\mathbf{v}, f, f] \quad (9)$$

is the *cooling rate* and

$$a_2(t) \equiv n \frac{d}{d+2} \frac{\int d\mathbf{v} v^4 f(\mathbf{v}; t)}{[\int d\mathbf{v} v^2 f(\mathbf{v}; t)]^2} \quad (10)$$

is the excess kurtosis (or fourth cumulant) of the time-dependent VDF. The coupling of $T(t)$ to $a_2(t)$ is a direct consequence of the quadratic term in the drag coefficient, which explicitly appears in the EFPE, Eq. (1). As for the cooling rate $\zeta(t)$, it is a consequence of inelasticity and, therefore, vanishes in the elastic case (conservation of energy). Insertion of Eq. (2) into Eq. (9) yields [18]

$$\zeta(t) = (1 - \alpha^2) \frac{v(t)}{\sqrt{2dn^2}} \frac{\Gamma\left(\frac{d}{2}\right)}{\Gamma\left(\frac{d+3}{2}\right)} \int d\mathbf{v}_1 \int d\mathbf{v}_2 \left[\frac{v_{12}}{v_{\text{th}}(t)} \right]^3 f(\mathbf{v}_1; t) f(\mathbf{v}_2; t). \quad (11)$$

Here, $v_{\text{th}}(t) = \sqrt{2T(t)/m}$ is the time-dependent thermal velocity and

$$v(t) = g_c K_d n \sigma^{d-1} v_{\text{th}}(t), \quad K_d \equiv \frac{\pi^{d-1}}{\sqrt{2}\Gamma(d/2)}, \quad (12)$$

is the time-dependent collision frequency.

Let us rewrite Eq. (8) in dimensionless form. First, we introduce the reduced quantities

$$t^* \equiv v_b t, \quad \theta(t^*) \equiv \frac{T(t)}{T_b}, \quad \xi_0^* \equiv \frac{\xi_0}{v_b}, \quad \mu_\ell(t^*) \equiv -\frac{1}{nv(t)} \int d\mathbf{v} \left[\frac{v}{v_{\text{th}}(t)} \right]^\ell J[\mathbf{v}|f, f], \quad (13)$$

where $v_b = g_c K_d n \sigma^{d-1} v_b$ is a collision frequency associated with the background temperature T_b . In terms of these quantities, Eq. (8) becomes

$$\frac{\dot{\theta}}{\xi_0^*} = 2(1 - \theta) [1 + (d+2)\gamma\theta] - 2(d+2)\gamma\theta^2 a_2 - \frac{2\mu_2}{d} \frac{\theta^{3/2}}{\xi_0^*}, \quad (14)$$

where henceforth a dot over a quantity denotes a derivative with respect to t^* and we have taken into account that $\zeta(t)/v(t) = 2\mu_2(t^*)/d$ and $v(t)/v_b = \theta^{1/2}$.

Equation (14) is not a closed equation since it is coupled to the full VDF through a_2 and μ_2 . More in general, taking velocity moments on the EFPE, an infinite hierarchy of moment equations can be derived. In dimensionless form, it reads

$$\frac{\dot{M}_\ell}{\xi_0^*} = \ell \left\{ \left[(\ell - 2)\gamma + \frac{\mu_2}{d} \frac{\sqrt{\theta}}{\xi_0^*} + (d + 2)\gamma\theta(1 + a_2) - \frac{1}{\theta} \right] M_\ell - 2\gamma\theta M_{\ell+2} + \frac{d + \ell - 2}{2} \frac{M_{\ell-2}}{\theta} \right\} - \mu_\ell \frac{\sqrt{\theta}}{\xi_0^*}, \quad (15)$$

where $M_\ell \equiv n^{-1} \int d\mathbf{v} (v/v_{\text{th}})^\ell f(\mathbf{v})$. In particular, $M_0 = 1$, $M_2 = \frac{d}{2}$, $M_4 = \frac{d(d+2)}{4}(1 + a_2)$, and $M_6 = \frac{d(d+2)(d+4)}{8}(1 + 3a_2 - a_3)$, a_3 being the sixth cumulant.

Equation (15) is trivial for $\ell = 0$ and $\ell = 2$. The choice $\ell = 4$ yields

$$\frac{\dot{a}_2}{\xi_0^*} = 4\gamma\theta \left[\frac{2(1 + a_2)}{\theta} + (d + 2)(1 + a_2)^2 - (d + 4)(1 + 3a_2 - a_3) \right] - 4\frac{a_2}{\theta} + \frac{4}{d} \left[\mu_2(1 + a_2) - \frac{\mu_4}{d + 2} \right] \frac{\sqrt{\theta}}{\xi_0^*}. \quad (16)$$

Equations (14)–(16) are formally exact in the context of the EFPE, Eq. (1). Nevertheless, they cannot be solved because of the infinite nature of the hierarchy (15) and the highly nonlinear dependence of the collisional moments μ_ℓ on the velocity moments of the VDF. This forces us to devise tractable approximations in order to extract information about the dynamics and steady state of the system.

3. Approximate Schemes

3.1. Maxwellian Approximation

The simplest approximation consists in assuming that the VDF remains very close to a Maxwellian during its time evolution, so that the excess kurtosis a_2 can be neglected in Eq. (14) and the reduced cooling rate μ_2 can be approximated by [11,12,17,18,28,31–33]

$$\mu_2 \approx \mu_2^{(0)} = 1 - \alpha^2. \quad (17)$$

In this Maxwellian approximation (MA), Eq. (14) becomes

$$\frac{\dot{\theta}}{\xi_0^*} \approx 2(1 - \theta) \left[1 + (d + 2)\gamma\theta \right] - \frac{2(1 - \alpha^2)}{d} \frac{\theta^{3/2}}{\xi_0^*}. \quad (18)$$

This is a closed equation for the temperature ratio $\theta(t^*)$ that can be solved numerically for any initial temperature. The steady-state value θ^{st} in the MA is obtained by equating to zero the right-hand side of Eq. (18), what results in a fourth-degree algebraic equation.

3.2. First Sonine Approximation

As we will see later, the MA given by Eq. (18) provides a simple and, in general, rather accurate estimate of $\theta(t^*)$ and θ^{st} . However, since the evolution of temperature is governed by its initial value only, the MA is unable to capture memory phenomena, such as Mpemba- or Kovacs-like effects, which are observed even in the case of elastic particles [21–23]. This is a consequence of the absence of any coupling of θ with some other dynamical variable(s).

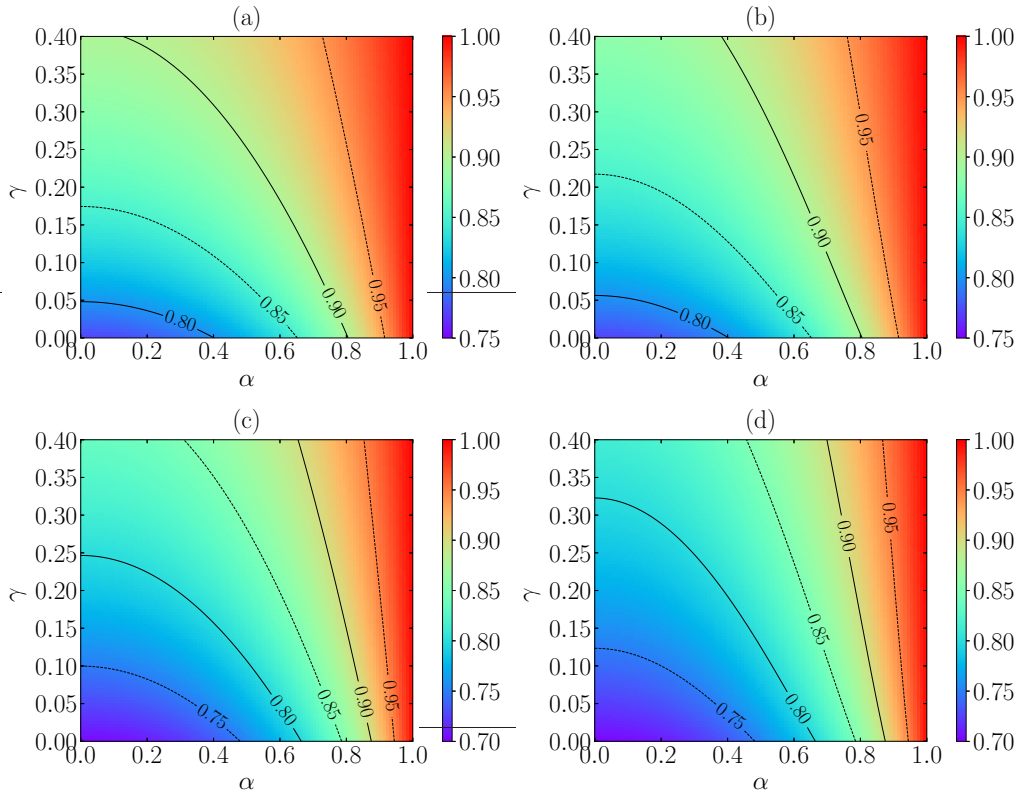


Figure 2. Theoretical predictions for the steady-state value of the reduced temperature θ^{st} as a function of the coefficient of normal restitution α and of the nonlinearity control parameter γ with $\zeta_0^* = 1$. Panels (a, c) correspond to the MA, while panels (b, d) correspond to the FSA. The dimensionality of the system is $d = 3$ in panels (a, b) and $d = 2$ in panels (c, d).

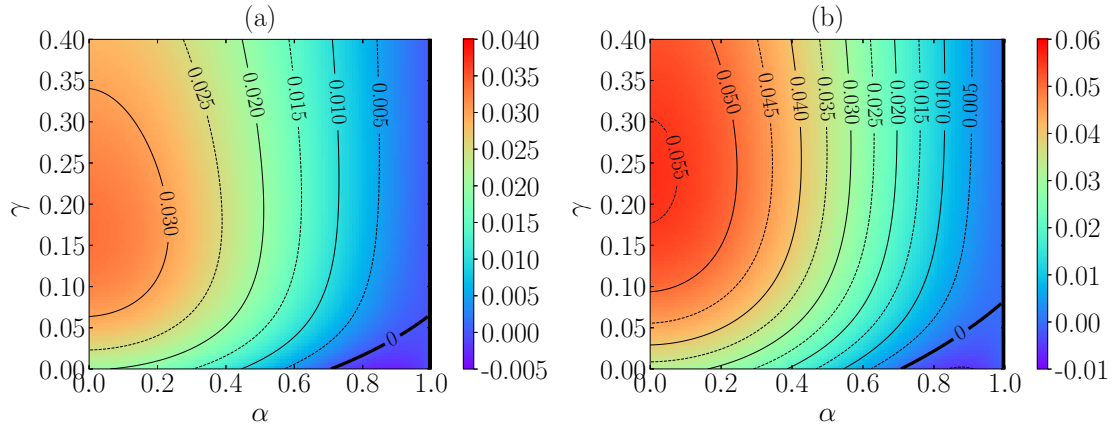


Figure 3. FSA predictions for the steady-state value of the excess kurtosis a_2^{st} as a function of the coefficient of normal restitution α and of the nonlinearity control parameter γ with $\zeta_0^* = 1$. The dimensionality of the system is $d = 3$ in panel (a) and $d = 2$ in panel (b). The thickest black line corresponds to the contour $a_2^{\text{st}} = 0$.

The next simplest approximation beyond the MA consists in incorporating a_2 into the description but assuming it is small enough as to neglect nonlinear terms involving this quantity, as well as

higher-order cumulants, i.e., $a_2^k \rightarrow 0$ for $k \geq 2$ and $a_\ell \rightarrow 0$ for $\ell \geq 3$. This represents the so-called first Sonine approximation (FSA), according to which Eqs. (14) and (16) become

$$\frac{\dot{\theta}}{\bar{\zeta}_0^*} \approx 2(1 - \theta) [1 + (d + 2)\gamma\theta] - 2(d + 2)\gamma\theta^2 a_2 - \frac{2 [\mu_2^{(0)} + \mu_2^{(1)} a_2] \theta^{3/2}}{d \bar{\zeta}_0^*}, \quad (19a)$$

$$\begin{aligned} \frac{\dot{a}_2}{\bar{\zeta}_0^*} \approx & 4\gamma\theta \left[2\frac{1+a_2}{\theta} + (d+2)(1+2a_2) - (d+4)(1+3a_2) \right] - 4\frac{a_2}{\theta} \\ & + \frac{4}{d} \left\{ \mu_2^{(0)} - \frac{\mu_4^{(0)}}{d+2} + \left[\mu_2^{(0)} + \mu_2^{(1)} - \frac{\mu_4^{(1)}}{d+2} \right] a_2 \right\} \frac{\sqrt{\theta}}{\bar{\zeta}_0^*}, \end{aligned} \quad (19b)$$

where we have used [11,12,17,18,28,31–33]

$$\mu_2 \approx \mu_2^{(0)} + \mu_2^{(1)} a_2, \quad \mu_4 \approx \mu_4^{(0)} + \mu_4^{(1)} a_2, \quad (20)$$

with

$$\begin{aligned} \mu_2^{(1)} &= \frac{3}{16} \mu_2^{(0)}, \quad \mu_4^{(0)} = \left(d + \frac{3}{2} + \alpha^2 \right) \mu_2^{(0)}, \\ \mu_4^{(1)} &= \frac{3}{32} (10d + 39 + 10\alpha^2) \mu_2^{(0)} + (d - 1)(1 + \alpha). \end{aligned} \quad (21)$$

Equations (19) make a set of two coupled differential equations. In contrast to the MA, now the evolution of $\theta(t^*)$ is governed by the initial values of both θ and a_2 . This latter fact implies that the evolution of temperature depends on the initial preparation of the whole VDF, this being a determinant condition for the emergence of memory effects, which will be explored later in Sec. 4.1.

3.2.1. Steady-State Values

The steady-state values θ^{st} and a_2^{st} in the FSA are obtained by equating to zero the right-hand sides of Eqs. (19), i.e.,

$$\dot{\theta} = 0 \Rightarrow F_0(\theta^{\text{st}}) + F_1(\theta^{\text{st}}) a_2^{\text{st}} = \left[\mu_2^{(0)} + \mu_2^{(1)} a_2^{\text{st}} \right] \frac{(\theta^{\text{st}})^{3/2}}{\bar{\zeta}_0^*}, \quad (22a)$$

$$a_2 = 0 \Rightarrow G_0(\theta^{\text{st}}) + G_1(\theta^{\text{st}}) a_2^{\text{st}} = \left\{ \frac{\mu_4^{(0)}}{d+2} - \mu_2^{(0)} + \left[\frac{\mu_4^{(1)}}{d+2} - \mu_2^{(0)} - \mu_2^{(1)} \right] a_2^{\text{st}} \right\} \frac{(\theta^{\text{st}})^{3/2}}{\bar{\zeta}_0^*}. \quad (22b)$$

where

$$F_0(\theta) = d(1 - \theta) [1 + (d + 2)\gamma\theta], \quad F_1(\theta) = -d(d + 2)\gamma\theta^2, \quad (23a)$$

$$G_0(\theta) = 2d\gamma\theta(1 - \theta), \quad G_1(\theta) = d\gamma\theta [2 - \theta(d + 8)] - d. \quad (23b)$$

Eliminating a_2^{st} in Eqs. (22), one gets a closed nonlinear equation for θ^{st} in our FSA. Once numerically solved, a_2^{st} is simply given by either Eq. (22a) or Eq. (22b). For instance, Eq. (22a) gives

$$a_2^{\text{st}} = - \frac{F_0(\theta^{\text{st}}) - \mu_2^{(0)} (\theta^{\text{st}})^{3/2} / \bar{\zeta}_0^*}{F_1(\theta^{\text{st}}) - \mu_2^{(1)} (\theta^{\text{st}})^{3/2} / \bar{\zeta}_0^*}. \quad (24)$$

Figure 2 compares the MA and FSA predictions of θ^{st} for three- and two-dimensional granular gases with $\bar{\zeta}_0^* = 1$. We observe that the breakdown of equipartition (as measured by $1 - \theta^{\text{st}}$) is stronger in 2D than in 3D and increases with increasing inelasticity but decreases as the nonlinearity

of the drag force grows. Apart from that, the deviations of the MA values with respect to the FSA ones increase with increasing nonlinearity and inelasticity, the MA values tending to be larger (i.e., closer to equipartition) than the FSA ones.

The FSA predictions of a_2^{st} are displayed in Fig. 3. First, it is quite apparent that the departure from the Maxwellian VDF (as measured by the magnitude of a_2^{st}) is higher in 2D than in 3D. It is also noteworthy that a_2^{st} starts growing with increasing γ , reaches a maximum at a certain value $\gamma = \gamma_{\text{max}}(\alpha, \zeta_0^*)$, and then it decreases as γ increases beyond $\gamma_{\text{max}}(\alpha, \zeta_0^*)$; this effect is more pronounced for small α .

Another interesting feature is that a_2^{st} takes negative values (in the domain of small inelasticity) only if γ is smaller than a certain value γ_c . Of course, $a_2^{\text{st}}(\alpha, \gamma)|_{\alpha=1} = 0$ for any γ (since the steady state with $\alpha = 1$ is that of equilibrium), but $\partial_\alpha a_2^{\text{st}}(\alpha, \gamma)|_{\alpha=1} < 0$ if $\gamma < \gamma_c$ and $\partial_\alpha a_2^{\text{st}}(\alpha, \gamma)|_{\alpha=1} > 0$ if $\gamma > \gamma_c$. Thus, the critical value γ_c is determined by the condition $\partial_\alpha a_2^{\text{st}}(\alpha, \gamma_c)|_{\alpha=1} = 0$. Interestingly, the result obtained from the FSA, Eq. (24), is quite simple, namely

$$\gamma_c = \frac{1}{3(d+2)}, \quad (25)$$

which is independent of ζ_0^* .

3.2.2. Special Limits

Absence of drag.

Let us first define a *noise temperature* T_n as $T_n = T_b \zeta_0^{*2/3} \propto (\zeta_0 T_b)^{2/3}$, so that $\theta^{3/2}/\zeta_0^* = (T/T_n)^{3/2}$. Now we take the limit of zero drag, $\zeta_0 \rightarrow 0$, with finite noise temperature T_n . This implies $T_b \rightarrow \infty$ and then the natural temperature scale of the problem is no longer T_b but T_n , i.e., $\theta^{\text{st}} \rightarrow 0$ but $T^{\text{st}}/T_n = \text{finite}$. From Eqs. (23) we see that $F_0(0) = d$, $F_1(0) = 0$, $G_0(0) = 0$, and $G_1(0) = -d$. Therefore, Eqs. (22) reduce to

$$\dot{\theta} = 0 \Rightarrow d \left(\frac{T_n}{T^{\text{st}}} \right)^{3/2} = \mu_2^{\text{st}}, \quad (26a)$$

$$a_2 = 0 \Rightarrow -d \left(\frac{T_n}{T^{\text{st}}} \right)^{3/2} a_2^{\text{st}} = \frac{\mu_4^{\text{st}}}{d+2} - \mu_2^{\text{st}}(1 + a_2^{\text{st}}), \quad (26b)$$

where, for the sake of generality, we have undone the linearizations with respect to a_2^{st} . By elimination of $(T_n/T^{\text{st}})^{3/2}$, one simply gets $(d+2)\mu_2^{\text{st}} = \mu_4^{\text{st}}$, from which one can then obtain a_2^{st} upon linearization [11,12]. The steady-state temperature is given by $T^{\text{st}}/T_n = (d/\mu_2^{\text{st}})^{2/3}$.

Homogeneous cooling state.

If, in addition to $\zeta_0 \rightarrow 0$, we take the limit $T_n \rightarrow 0$, the asymptotic state becomes the homogeneous cooling state. In that case, T does not reach a true stationary value, but a_2 does. As a consequence, Eq. (26a) is not applicable, but Eq. (26b), with $T_n = 0$, can still be used to get $(d+2)\mu_2^{\text{st}}(1 + a_2^{\text{st}}) = \mu_4^{\text{st}}$, as expected [11,12,17].

Linear drag force: $\gamma = 0$.

If the drag force is linear in velocity (i.e., $\gamma = 0$), we have $F_0(\theta) = d(1 - \theta)$, $F_1(\theta) = 0$, $G_0(\theta) = 0$, and $G_1(\theta) = -d$. Using Eq. (22b), a_2^{st} is given by

$$a_2^{\text{st}} = -\frac{\mu_4^{(0)} - (d+2)\mu_2^{(0)}}{\mu_4^{(0)} - (d+2) \left[\mu_2^{(0)} + \mu_2^{(1)} - d\zeta_0^*/(\theta^{\text{st}})^{3/2} \right]}, \quad (27)$$

thus recovering previous results [34].

4. Comparison with Computer Simulations

We have carried out DSMC and EDMD computer simulations to validate the theoretical predictions. The DSMC method is based on the acceptance-rejection Monte Carlo Metropolis decision method [35] but adapted to solve the Enskog–Boltzmann equation [36,38], and the algorithm is consequently adapted to agree with the inelastic collisional model [12,17] and reflects the interaction with the bath [23]. On the other hand, the EDMD algorithm is based on the one exposed in Ref. [23], but adjusted to the IHS collisional model. The main difference between DSMC and EDMD is that the latter does not follow any statistical rule to solve the Boltzmann equation, but solves the equations of motion of the hard particles. We refer the reader to Ref. [23] for further technical details on the employed simulation schemes.

In Fig. 4, results from simulations are compared with the theoretical predictions of θ^{st} from MA and FSA, and of a_2^{st} from FSA, in a three-dimensional ($d = 3$) IHS system with $\zeta_0^* = 1$. It can be observed that both DSMC and EDMD results agree with each other. From panel 4(a) one can conclude that, as expected, FSA works in the prediction of θ^{st} much better than MA for values of γ close to $\gamma_{\max}(\alpha, \zeta_0^*)$ (which corresponds to the maximum magnitude of a_2^{st}). Moreover, FSA gives reasonably good estimates for the values of a_2^{st} , although they get worse for increasing inelasticity, i.e., decreasing α . One might also think that the increase of γ produces a poorer approach; however, according to theory, the performance of FSA improves if $\gamma > \gamma_{\max}(\alpha, \zeta_0^*)$, which corresponds to a decrease of $|a_2^{\text{st}}|$. Of course, nonlinear terms or higher-order cumulants might play a role that it is not accounted for within FSA.

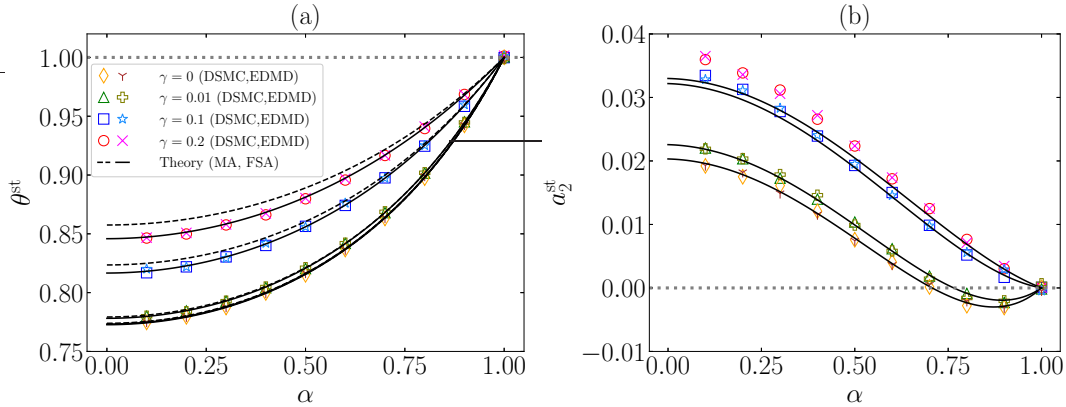


Figure 4. Plots of the steady-state values of (a) the temperature ratio θ^{st} and (b) the excess kurtosis a_2^{st} vs the coefficient of normal restitution α for $\zeta_0^* = 1$, $d = 3$, and different values of the nonlinearity parameter: $\gamma = 0, 0.01, 0.1, 0.2$. The symbols stand for DSMC ($\diamond, \triangle, \square, \circ$) and EDMD ($Y, +, *, \times$) simulation results, respectively. Dashed (– –) and solid (—) lines refer to MA [only in panel (a)] and FSA predictions, respectively. The horizontal gray dotted lines (\cdots) correspond to the steady-state values in the elastic limit.

Apart from the steady-state values, we have studied the temporal evolution of θ and a_2 , starting from a Maxwellian VDF at temperature T_b , i.e., $\theta(0) \equiv \theta^0 = 1$ and $a_2(0) \equiv a_2^0 = 0$. Note that this state is that of equilibrium in the case of elastic collisions ($\alpha = 1$), regardless of the value of the nonlinearity parameter γ . The theoretical and simulation results are displayed in Fig. 5 for $d = 3$, $\zeta_0^* = 1$, and some characteristic values of α and γ .

We observe that the relaxation of θ is accurately predicted by MA, except for the later stage with small α and/or large γ , in accordance with the discussion of Fig. 4. This is remedied by FSA, which exhibits an excellent agreement with simulation results in the case of θ and a fair agreement in the case of a_2 , again in accordance with the discussion of Fig. 4. It is also worthwhile mentioning the

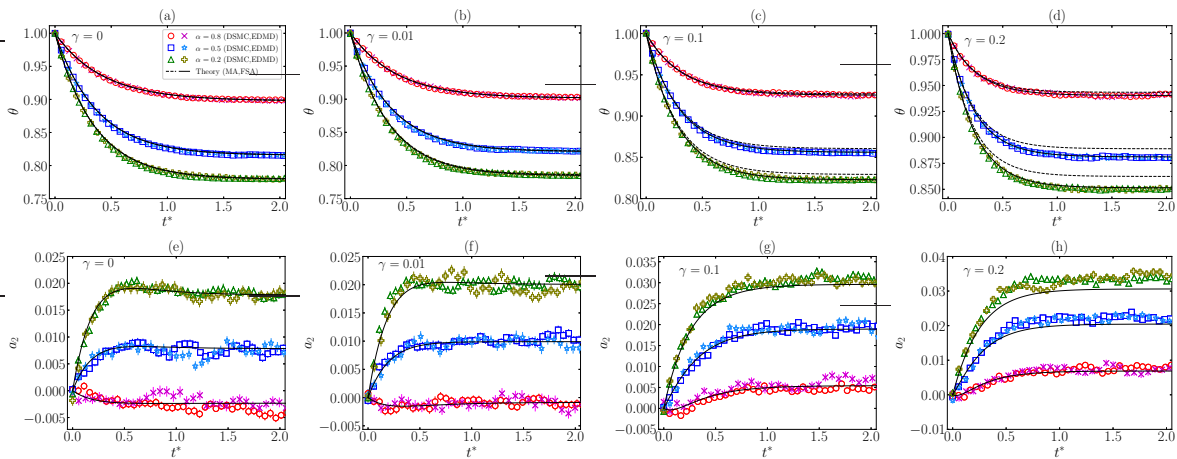


Figure 5. Plots of the time evolution of (a, b, c, d) the temperature ratio $\theta(t^*)$ and (e, f, g, h) the excess kurtosis $a_2(t^*)$ for $\zeta_0^* = 1$, $d = 3$, and different values of the coefficient of normal restitution ($\alpha = 0.8, 0.5, 0.2$) and the nonlinearity parameter: (a, e) $\gamma = 0$, (b, f) $\gamma = 0.01$, (c, g) $\gamma = 0.1$, and (d, h) $\gamma = 0.2$. The symbols stand for DSMC ($\circ, \square, \triangle$) and EDMD ($\times, *, +$) simulation results, respectively. Dashed (---) and solid (—) lines refer to MA [only in panels (a, b, c, d)] and FSA predictions, respectively. All states are initially prepared with a Maxwellian VDF at the bath temperature, i.e., $\theta^0 = 1$ and $a_2^0 = 0$.

good mutual agreement between DSMC and EDMD data, even though fluctuations are much higher in a_2 than in θ because of the rather small values of $|a_2|$.

4.1. Memory Effects

Whereas the temperature relaxation from Maxwellian initial states is generally accurate from MA, it misses the explicit dependence of the temperature evolution on the fourth cumulant [see Eq. 14], which, however, is captured by FSA [see Eq. (19a)]. This coupling of θ to a_2 is a signal of preparation dependence of the system, hence, a signal of memory effects, as occurs in the elastic case reported in Refs. [21–23].

4.1.1. Mpemba Effect

We start the study of memory effects with the Mpemba effect [39–43]. This counterintuitive phenomenon refers to situations in which an initially hotter sample (A) of a fluid—or, more generally, a statistical-mechanical system—cools down sooner than an initially colder one (B) in a cooling experiment. We will refer to this as the direct Mpemba effect (DME). Analogously, the inverse Mpemba effect (IME) occurs in heating experiments if the initially colder sample (B) heats up more rapidly than the initially hotter one (A) [21,23,41,42,44]. In the special case of a molecular gas (i.e., $\alpha = 1$) an extensive study of both the DME and the IME has recently been carried out [21,23].

Figures 6(a) and 6(b) present an example of DME and IME, respectively. As expected, FSA describes very well the evolution and crossing for temperatures of samples A and B. On the contrary, MA does not predict this memory effect. In addition, from Figs. 6(c, d) we can conclude that FSA captures quite well the relaxation of a_2 toward $a_2^{\text{st}} \neq 0$.

4.1.2. Kovacs Effect

Next, we turn to another interesting memory effect: the Kovacs effect [45,46]. In contrast to the Mpemba effect, the Kovacs effect has a well-defined two-stage protocol and does not involve a comparison between two samples. In the context of our system, it is first put in contact with a bath at temperature T_{b1} and initialized at a temperature $T^0 > T_1^{\text{st}}$, T_1^{st} being the corresponding steady-state temperature (note that $\theta_1^{\text{st}} = T_1^{\text{st}}/T_{b1}$ depends on T_{b1} through the reduced coefficient ζ_0^*). The system

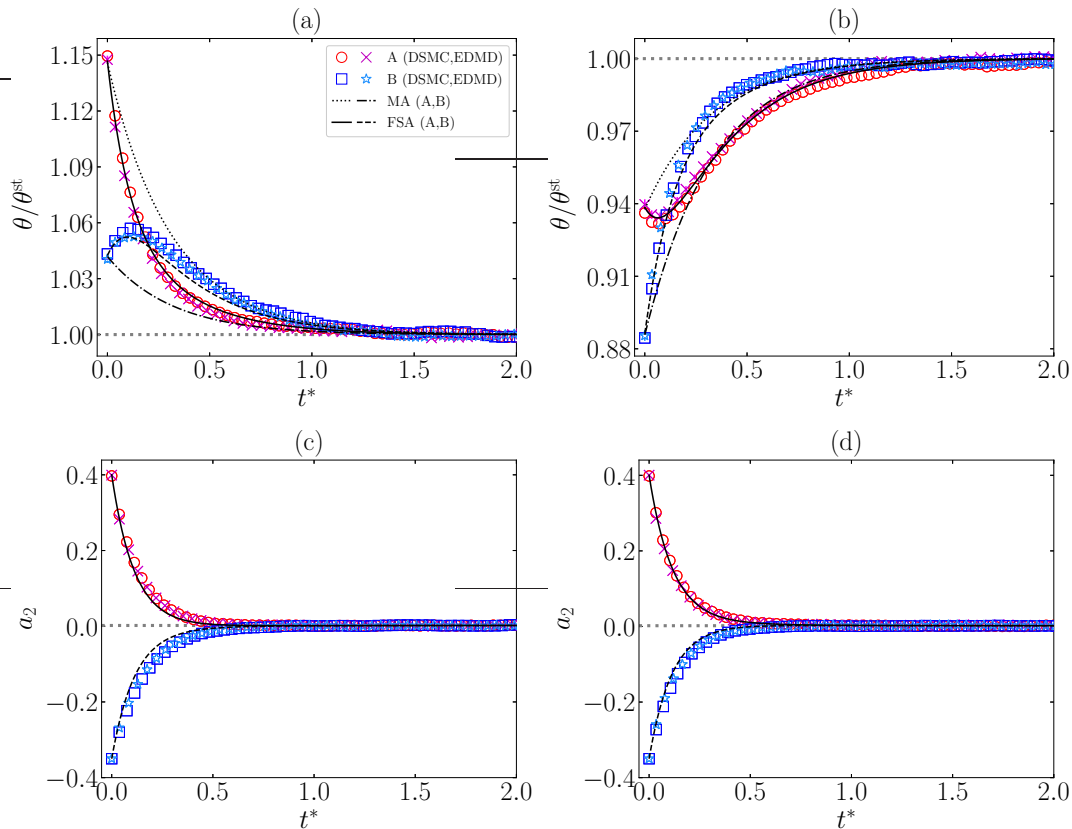


Figure 6. Time evolution of (a, b) $\theta(t^*)/\theta^{\text{st}}$ and (c, d) $a_2(t^*)$ for two samples (A and B) with $\alpha = 0.9$, $\zeta_0^* = 1$, $d = 3$, and $\gamma = 0.1$. Panels (a, c) illustrate the DME with initial conditions $\theta_A^0 = 1.1 \simeq 1.15\theta^{\text{st}}$, $a_{2A}^0 = 0.4$, $\theta_B^0 = 1 \simeq 1.04\theta^{\text{st}}$, $a_{2B}^0 = -0.35$, while panels (b, d) illustrate the IME with initial conditions $\theta_A^0 = 0.9 \simeq 0.94\theta^{\text{st}}$, $a_{2A}^0 = 0.4$, $\theta_B^0 = 0.85 \simeq 0.89\theta^{\text{st}}$, $a_{2B}^0 = -0.35$. The symbols stand for DSMC (\circ , \square) and EDMD (\times , $*$) simulation results, respectively. Solid (—) and dashed (---) lines corresponds to FSA predictions for samples A and B, respectively, whereas black dotted (\cdots) and dash-dotted ($- \cdot -$) lines in panels (a, b) refer to MA predictions for samples A and B, respectively. The gray thin horizontal lines correspond to the steady-state values. Note that $a_2^{\text{st}} \neq 0$, despite what panels (c, d) seem to indicate because of the vertical scale.

is allowed to relax to the steady state during a time window $0 < t < t_K$, but then, at $t = t_K$, the bath temperature is suddenly modified to a new value T_b , such that $T(t_K) = T^{\text{st}}$, T^{st} being the new steady-state value. If the system did not keep memory of its previous history, one would have $T(t) = T^{\text{st}}$ for $t > t_K$ and this is in fact the result given by the MA. However, the temperature exhibits a hump for $t > t_K$, before relaxing to T^{st} . This hump is a consequence of the dependence of $\partial_t T$ on inner variables of the system. According to Eq. (14), and maintained in the FSA, Eq. (19a), the first relevant quantity to be responsible for a possible hump is the excess kurtosis of the VDF, as occurs in the elastic limit [22].

For simplicity, in our study of the Kovacs-like effect, we replace the first stage of the protocol ($0 < t^* < t_K^*$) by just generating the state at $t^* = t_K^*$ with $\theta(t_K^*) = \theta^{\text{st}}$ and $a_2(t_K^*) \neq a_2^{\text{st}}$. The effect is illustrated in Fig. 7 for the same system as in Fig. 6 with the choices $a_2(t_K^*) = -0.35 < a_2^{\text{st}}$ and $a_2(t_K^*) = 0.4 > a_2^{\text{st}}$. In the former, the hump points upward, while it points downward in the latter. Again, DSMC and EDMD results agree between each other and with theoretical predictions. However, in the case $a_2(t_K^*) = -0.35$ (upward hump), Fig. 7(a), we observe that the theoretical curve lies below the simulation results. This might be caused by a nonnegligible value of the sixth cumulant at $t^* = t_K^*$, $a_3(t_K^*) = -0.375$, as reported in Ref. [23] in the elastic case. Apart from this small discrepancy, FSA

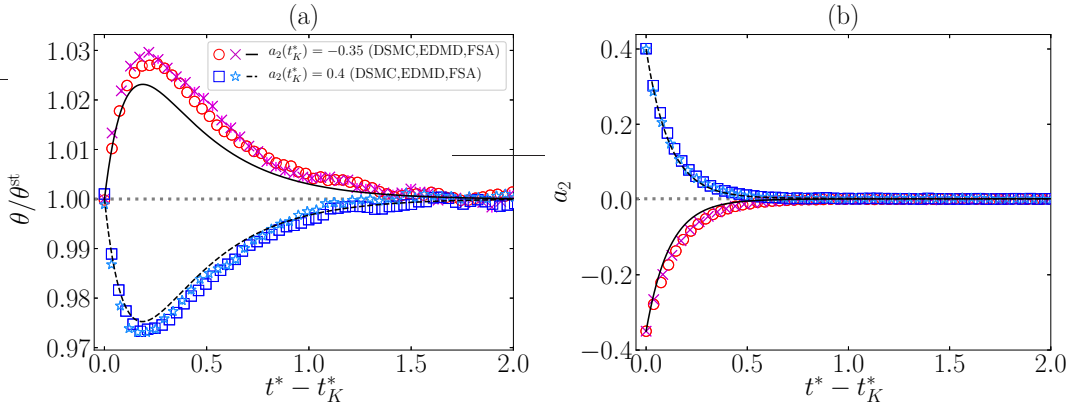


Figure 7. Time evolution for $t^* > t_K^*$ of (a) $\theta(t^*)/\theta^{\text{st}}$ and (b) $a_2(t^*)$ for a system with $\alpha = 0.9$, $\zeta_0^* = 1$, $d = 3$, and $\gamma = 0.1$. The figure illustrates Kovacs-like effects with conditions $\theta(t_K^*) = \theta^{\text{st}}$ and either $a_2(t_K^*) = -0.35$ (\circ , \square , $-$) or $a_2(t_K^*) = 0.4$ (\times , $*$, $- -$). The symbols stand for DSMC and EDMD simulation results, while lines refer to FSA predictions.

captures very well the magnitude and sign of the humps, as well as the relaxation of the fourth cumulant.

5. Conclusions

In this work, we have looked into the dynamics of a dilute granular gas immersed in a thermal bath, at a temperature T_b , made of smaller particles but with masses comparable as those of the grains. To characterize mathematically this system, we have worked under the assumptions of Boltzmann's kinetic theory, describing the system by the one-particle VDF, whose evolution is monitored by the EFPE, Eq. (1). In addition, we have assumed that the evolution due to collisions is determined by binary encounters only, collision rules following the IHS model for hard d -spheres. The action of the bath on the dynamics of the granular gas is modeled by a nonlinear drag force and an associated stochastic force. At a given dimensionality d , the control parameters of the problem are the coefficient of normal restitution (α), the (reduced) drag coefficient at zero velocity (ζ_0^*), and the nonlinearity parameter (γ).

After a general derivation of the kinetic theory description. in Sec. 2, we obtain the evolution equation of the reduced temperature $\theta(t^*) \equiv T(t^*)/T_b$ [Eq. (14)], which is coupled explicitly to the excess kurtosis evolution, a_2 , and depends on every VDF moment through the second collisional moment μ_2 (which is nonzero due to inelasticity). Therefore, the whole dynamics in the context of the EFPE is formally described by Eq. (14) and the infinite hierarchy of moment equations given by Eq. (15). However, in order to give predictions, we have proposed two approximations. The first one is MA, which consists in assuming a Maxwellian for the one-particle VDF, whereas the second one, FSA, consists in truncating a Sonine expansion of the VDF up to the first nontrivial cumulant a_2 . Their evolution equations are given by Eqs. (18) and (19), respectively. The predictions for the steady-state values are exposed in Figs. 2 and 3, which show some small discrepancies in θ^{st} between MA and FSA as we increase inelasticity (decreasing α). Moreover, we observed that, for fixed α and ζ_0^* , a_2^{st} gets its maximum value when the nonlinearity parameter is $\gamma = \gamma_{\text{max}}(\alpha, \zeta_0^*)$. Another interesting feature is the existence of a critical value of the nonlinearity parameter, γ_c , such that for $\gamma > \gamma_c$ the values of a_2^{st} are always positive for every value of α , while for $\gamma < \gamma_c$ we find $a_2^{\text{st}} < 0$ for small inelasticities. Interestingly, the value of γ_c given by Eq. (25) is found to be independent of ζ_0^* . In addition, some already known limits are recovered in Sec. 3.2.2.

Furthermore, in order to check the predictions from MA and FSA equations, we carried out DSMC and EDMD simulations for hard spheres ($d = 3$) with fixed $\zeta_0^* = 1$ (which corresponds to comparable time scales associated with drag and collisions). First, from Fig. 4(a) we can conclude

that, whereas MA provides good predictions of θ^{st} , except for large inelasticities and values of γ close to γ_{max} , FSA is much more accurate because it takes into account the influence of a_2^{st} . The latter approach is generally reliable for a_2^{st} , as observed in Fig. 4(b), although, not unexpectedly, it slightly worsens as $|a_2^{\text{st}}|$ grows. Relaxation curves starting from a Maxwellian initial state in Fig. 5 show that FSA agrees very well with both DSMC and EDMD; however, MA exhibits a good agreement during the first stage of the evolution but becomes less reliable as the steady state is approached.

A relevant feature of these systems, as already studied in the elastic case [21–23], is the emergence of memory effects, which are not contemplated by MA. FSA predicts very well the emergence of the Mpemba effect, both DME and IME, as can be seen in Fig. 6. Analogously, Kovacs-like humps, both upward and downward, are correctly described by FSA, as observed in Fig. 7, although the FSA humps are slightly less pronounced (especially the upward one) than the simulations ones. This is presumably due to the role played by a_3 and higher-order cumulants, as occurs in the elastic limit reported in Ref. [23].

To conclude, we expect this work motivates research about this type of systems and the emergence of memory effects. For instance, one can extend the study to other collisional models (like that of rough spheres), to nonhomogeneous states, or to a more detailed description of the memory effects observed.

Author Contributions: A.M. worked out the approximations and performed the simulations, and A.S. supervised the work. Both authors participated in the analysis and discussion of the results and worked on the revision and writing of the final manuscript. All authors have read and agreed to the published version of the manuscript.

Funding: The authors acknowledge financial support from Grant No. PID2020-112936GB-I00 funded by MCIN/AEI/10.13039/501100011033, and from Grants No. IB20079 and No. GR21014 funded by Junta de Extremadura (Spain) and by ERDF “A way of making Europe.” A.M. is grateful to the Spanish Ministerio de Ciencia, Innovación y Universidades for a predoctoral fellowship FPU2018-3503.

Conflicts of Interest: The authors declare no conflict of interest.

Abbreviations

The following abbreviations are used in this manuscript:

DME	Direct Mpemba effect
DSMC	Direct simulation Monte Carlo
EDMD	Event-driven molecular dynamics
EFPE	Enskog–Fokker–Planck equation
FSA	First Sonine approximation
IHS	Inelastic hard spheres
IME	Inverse Mpemba effect
MA	Maxwellian approximation
VDF	Velocity distribution function

References

1. Tatsumi, S.; Murayama, Y.; Hayakawa, H.; Sano, M. Experimental study on the kinetics of granular gases under microgravity. *J. Fluid Mech.* **2009**, *641*, 521–539. <https://doi.org/10.1017/S002211200999231X>.
2. Yu, P.; Schröter, M.; Sperl, M. Velocity Distribution of a Homogeneously Cooling Granular Gas. *Phys. Rev. Lett.* **2020**, *124*, 208007. <https://doi.org/10.1103/PhysRevLett.124.208007>.
3. Pouliquen, O.; Nicolas, M.; Weidman, P.D. Crystallization of non-Brownian Spheres under Horizontal Shaking. *Phys. Rev. Lett.* **1997**, *79*, 3640–3643. <https://doi.org/10.1103/PhysRevLett.79.3640>.
4. Tennakoon, S.G.K.; Behringer, R.P. Vertical and Horizontal Vibration of Granular Materials: Coulomb Friction and a Novel Switching State. *Phys. Rev. Lett.* **1998**, *81*, 794–797. <https://doi.org/10.1103/PhysRevLett.81.794>.

5. Metcalfe, G.; Tennakoon, S.G.K.; Kondic, L.; Schaeffer, D.G.; Behringer, R.P. Granular friction, Coulomb failure, and the fluid-solid transition for horizontally shaken granular materials. *Phys. Rev. E* **2002**, *65*, 031302. <https://doi.org/10.1103/PhysRevE.65.031302>.
6. Huan, C.; Yang, X.; Candela, D.; Mair, R.W.; Walsworth, R.L. NMR experiments on a three-dimensional vibrofluidized granular medium. *Phys. Rev. E* **2004**, *69*, 041302. <https://doi.org/10.1103/PhysRevE.69.041302>.
7. Schröter, M.; Goldman, D.I.; Swinney, H.L. Stationary state volume fluctuations in a granular medium. *Phys. Rev. E* **2005**, *71*, 030301. <https://doi.org/10.1103/PhysRevE.71.030301>.
8. Abate, A.R.; Durian, D.J. Approach to jamming in an air-fluidized granular bed. *Phys. Rev. E* **2006**, *74*, 031308. <https://doi.org/10.1103/PhysRevE.74.031308>.
9. Eshuis, P.; van der Meer, D.; Alam, M.; van Gerner, H.J.; van der Weele, K.; Lohse, D. Onset of Convection in Strongly Shaken Granular Matter. *Phys. Rev. Lett.* **2010**, *104*, 038001. <https://doi.org/10.1103/PhysRevLett.104.038001>.
10. Michael, B.; Simon, M.; Gustavo, C.; Eric, F. Wave spectroscopy in a driven granular material. *Proc. R. Soc. A* **2022**, *476*, 20220014. <https://doi.org/10.1098/rspa.2022.0014>.
11. van Noije, T.P.C.; Ernst, M.H. Velocity distributions in homogeneous granular fluids: the free and the heated case. *Granul. Matter* **1998**, *1*, 57–64. <https://doi.org/10.1007/s100350050009>.
12. Montanero, J.M.; Santos, A. Computer simulation of uniformly heated granular fluids. *Granul. Matter* **2000**, *2*, 53–64. <https://doi.org/10.1007/s100350050035>.
13. Garzó, V.; Chamorro, M.G.; Vega Reyes, F. Transport properties for driven granular fluids in situations close to homogeneous steady states. *Phys. Rev. E* **2013**, *87*, 032201. **87**, 059906(E) (2013).
14. Vega Reyes, F.; Santos, A. Steady state in a gas of inelastic rough spheres heated by a uniform stochastic force. *Phys. Fluids* **2015**, *27*, 113301. <https://doi.org/10.1063/1.4934727>.
15. Brey, J.J.; Buzón, V.; Maynar, P.; García de Soria, M.I. Hydrodynamics for a model of a confined quasi-two-dimensional granular gas. *Phys. Rev. E* **2015**, *91*, 052201. <https://doi.org/10.1103/PhysRevE.91.052201>.
16. Garzó, V.; Brito, R.; Soto, R. Enskog kinetic theory for a model of a confined quasi-two-dimensional granular fluid. *Phys. Rev. E* **2018**, *98*, 052904. <https://doi.org/10.1103/PhysRevE.98.052904>.
17. Santos, A.; Montanero, J.M. The second and third Sonine coefficients of a freely cooling granular gas revisited. *Granul. Matter* **2009**, *11*, 157–168. <https://doi.org/10.1007/s10035-009-0132-8>.
18. Garzó, V. *Granular Gaseous Flows. A Kinetic Theory Approach to Granular Gaseous Flows*; Springer Nature: Switzerland, 2019.
19. Megías, A.; Santos, A. Driven and undriven states of multicomponent granular gases of inelastic and rough hard disks or spheres. *Granul. Matter* **2019**, *21*, 49. <https://doi.org/10.1007/s10035-019-0901-y>.
20. Gómez González, R.; Garzó, V. Kinetic theory of granular particles immersed in a molecular gas. *J. Fluid Mech.* **2022**, *943*, A9. <https://doi.org/10.1017/jfm.2022.410>.
21. Santos, A.; Prados, A. Mpemba effect in molecular gases under nonlinear drag. *Phys. Fluids* **2020**, *32*, 072010. <https://doi.org/10.1063/5.0016243>.
22. Patrón, A.; Sánchez-Rey, B.; Prados, A. Strong nonexponential relaxation and memory effects in a fluid with nonlinear drag. *Phys. Rev. E* **2021**, *104*, 064127. <https://doi.org/10.1103/PhysRevE.104.064127>.
23. Megías, A.; Santos, A.; Prados, A. Thermal versus entropic Mpemba effect in molecular gases with nonlinear drag. *Phys. Rev. E* **2022**, *105*, 054140. <https://doi.org/10.1103/PhysRevE.105.054140>.
24. Ferrari, L. Particles dispersed in a dilute gas: Limits of validity of the Langevin equation. *Chem. Phys.* **2007**, *336*, 27–35. <https://doi.org/10.1016/j.chemphys.2007.05.001>.
25. Ferrari, L. Particles dispersed in a dilute gas. II. From the Langevin equation to a more general kinetic approach. *Chem. Phys.* **2014**, *428*, 144–155. <https://doi.org/10.1016/j.chemphys.2013.10.024>.
26. Hohmann, M.; Kindermann, F.; Lausch, T.; Mayer, D.; Schmidt, F.; Lutz, E.; Widera, A. Individual Tracer Atoms in an Ultracold Dilute Gas. *Phys. Rev. Lett.* **2017**, *118*, 263401. <https://doi.org/10.1103/PhysRevLett.118.263401>.
27. Brilliantov, N.; Pöschel, T. Deviation from Maxwell distribution in granular gases with constant restitution coefficient. *Phys. Rev. E* **2000**, *61*, 2809–2812. <https://doi.org/10.1103/PhysRevE.61.2809>.
28. Brilliantov, N.V.; Pöschel, T. *Kinetic Theory of Granular Gases*; Oxford University Press: Oxford, 2004.

29. Vega Reyes, F.; Santos, A.; Kremer, G.M. Role of roughness on the hydrodynamic homogeneous base state of inelastic spheres. *Phys. Rev. E* **2014**, *89*, 020202(R). <https://doi.org/10.1103/PhysRevE.89.020202>.
30. Megías, A.; Santos, A. Kullback–Leibler divergence of a freely cooling granular gas. *Entropy* **2020**, *22*, 1308. <https://doi.org/10.3390/e22040469>.
31. Goldshtein, A.; Shapiro, M. Mechanics of collisional motion of granular materials. Part 1. General hydrodynamic equations. *J. Fluid Mech.* **1995**, *282*, 75–114. <https://doi.org/10.1017/S0022112095000048>.
32. Brilliantov, N.; Pöschel, T. Breakdown of the Sonine expansion for the velocity distribution of granular gases. *Europhys. Lett.* **2006**, *74*, 424–430. Erratum: **75**, 188 (2006), <https://doi.org/10.1209/epl/i2005-10555-6>.
33. Brilliantov, N.; Pöschel, T. Erratum: Breakdown of the Sonine expansion for the velocity distribution of granular gases. *Europhys. Lett.* **2006**, *75*, 188–188. <https://doi.org/10.1209/epl/i2006-10099-3>.
34. Chamorro, M.G.; Vega Reyes, F.; Garzó, V. Homogeneous states in granular fluids driven by thermostats. *AIP Conf. Proc.* **2012**, *1501*, 1024–1030. <https://doi.org/10.1063/1.4769654>.
35. Metropolis, N.; Rosenbluth, A.W.; Rosenbluth, M.N.; Teller, A.H.; Teller, E. Equation of State Calculations by Fast Computing Machines. *J. Chem. Phys.* **1953**, *21*, 1087–1092. <https://doi.org/10.1063/1.1699114>.
36. Bird, G.A. *Molecular Gas Dynamics and the Direct Simulation of Gas Flows*; Clarendon: Oxford, UK, 1994.
37. Montanero, J.M.; Santos, A. *Phys. Fluids* **1997**, *9*, 2057.
38. Bird, G.A. *The DSMC Method*; CreateSpace Independent Publishing Platform: Scotts Valley, CA, 2013.
39. Mpemba, E.B.; Osborne, D.G. Cool? *Phys. Educ.* **1969**, *4*, 172–175. <https://doi.org/10.1088/0031-9120/4/3/312>.
40. BurrIDGE, H.C.; Linden, P.F. Questioning the Mpemba effect: hot water does not cool more quickly than cold. *Sci. Rep.* **2016**, *6*, 37665. <https://doi.org/10.1038/srep37665>.
41. Lu, Z.; Raz, O. Nonequilibrium thermodynamics of the Markovian Mpemba effect and its inverse. *Proc. Natl. Acad. Sci. U.S.A.* **2017**, *114*, 5083–5088. <https://doi.org/10.1073/pnas.1701264114>.
42. Lasanta, A.; Vega Reyes, F.; Prados, A.; Santos, A. When the Hotter Cools More Quickly: Mpemba Effect in Granular Fluids. *Phys. Rev. Lett.* **2017**, *119*, 148001. <https://doi.org/10.1103/PhysRevE.99.060901>.
43. Bechhoefer, J.; Kumar, A.; Chétrite, R. A fresh understanding of the Mpemba effect. *Nat. Rev. Phys.* **2021**, *3*, 534–535. <https://doi.org/10.1038/s42254-021-00349-8>.
44. Gómez González, R.; Khalil, N.; Garzó, V. Mpemba-like effect in driven binary mixtures. *Phys. Fluids* **2021**, *33*, 053301. <https://doi.org/10.1063/5.0050530>.
45. Kovacs, A.J. Transition vitreuse dans les polymères amorphes. Etude phénoménologique. *Fortschr. Hochpolym.-Forsch.* **1963**, *3*, 394–507. <https://doi.org/10.1007/BFb0050366>.
46. Kovacs, A.J.; Aklonis, J.J.; Hutchinson, J.M.; Ramos, A.R. Isobaric volume and enthalpy recovery of glasses. II. A transparent multiparameter theory. *J. Polym. Sci. Polym. Phys. Ed.* **1979**, *17*, 1097–1162. <https://doi.org/10.1002/pol.1979.180170701>.